Synthesis of CuInS$_2$ nanowire arrays via solution transformation of Cu$_2$S self-template for enhanced photoelectrochemical performance

Ming Li, Renjie Zhao, Yanjie Su*, Jing Hu, Zhi Yang, Yafei Zhang*

Key Laboratory for Thin Film and Microfabrication of the Ministry of Education, Department of Micro/Nano Electronics, School of Electronic Information and Electrical Engineering, Shanghai Jiao Tong University, Shanghai 200240, PR China

ARTICLE INFO

ABSTRACT

A novel universal solution method has been proposed to prepare CuInS$_2$ nanowire arrays (NWAs) using Cu$_2$S NWAs as the template. The screw-like CuInS$_2$ nanowires are constructed by many stacked nanoplates oriented along the direction of [221], and show diameters of 400–700 nm and lengths of several micrometres. Experimental results suggest that relatively higher In^{3+} concentration is beneficial to the insertion of In^{3+} into Cu$_2$S to form CuInS$_2$ with conserving the nanowire morphology. A novel exchange-erosion formation mechanism is proposed to illustrate the formation of the screw-like CuInS$_2$ NWAs. The photoelectrochemical (PEC) performance has been investigated using the CuInS$_2$ NWAs as photocathodes, and they exhibit double-increased photocurrent (0.3 mA cm^{-2} at −0.1 V *vs.* RHE) compared to the pristine Cu$_2$S NWAs, which can be ascribed to the enhanced light absorption and increased contact area for fast interfacial photocarrier separation and PEC reactions. The photocurrent has been further increased to 0.71 mA cm^{-2} *via* decorating CdS quantum dots on the surfaces of CuInS$_2$ nanowires. It is believed that this facile method can be generalized to prepare other copper chalcopyrite-based NWAs for highly efficient PEC water splitting.

© 2016 Published by Elsevier B.V.

1. Introduction

Solar-driven photoelectrochemical (PEC) water splitting has attracted considerable attention as an efficient way to produce carbon-free fuels from solar energy [1,2]. Since the pioneering work by Fujishima and Honda in the early 1970s [3], various semiconductors have been intensively studied as photoelectrodes for efficient solar-to-hydrogen conversion in the past forty years [4–7]. In terms of hydrogen generation, *p*-type semiconductors are advantageous over *n*-type ones because the photo-generated electrons can be directly injected into the electrolyte on semiconductors and thus directly reduce water to hydrogen at the semiconductor/water interface without potential energy loss [8]. However, the number of inherent *p*-type semiconductors is relatively small.

Due to their high absorption coefficients, relatively high carrier mobility, tunable band gap values, and suitable band alignment for water reduction, copper-based chalcopyrite *p*-type semiconductors such as CuInSe$_2$, CuGaSe$_2$, CuInS$_2$, CuGaS$_2$, and their mixed crystals have received great attentions as photocathodes for PEC water splitting [9–13]. Especially, CuInS$_2$ is a semiconductor with

a direct band gap of ∼1.5 eV, allowing it utilize sunlight efficiently and without requiring a highly toxic Se source [14,15]. Additionally, the CuInS$_2$-based solar cells show a high theoretical solar energy conversion efficiency of ∼25% [16], and the highest efficiency has been reported to be 11.4% [17]. The specific properties of CuInS$_2$ demonstrate that this semiconductor is attractive as an efficient photocathode for hydrogen production by PEC water reduction. Among various routes to prepare CuInS$_2$ photocathodes for efficient PEC water reduction, non-vacuum methods have attracted much attention owing to their low-cost fabrication processes [15,18]. However, the corresponding CuInS$_2$ photocathodes have shown relatively low PEC performance [19].

To realize highly efficient PEC cells, a nanostructured photoelectrode possesses favourable intrinsic characteristics of large specific surface area, direct electron transport pathway, and enhanced light absorption ability [20–24]. Luo *et al.* [25] developed a low-cost solution method to fabricate nanostructured CuInS$_2$ electrodes by solvothermal treatment of electrochemically deposited Cu$_2$O films, which showed excellent PEC water splitting ability after coating with CdS, Al-doped ZnO and TiO$_2$ overlayers. Domen et al. [15] reported the preparation of porous CuInS$_2$ by sulfurization of electrodeposited metals, which also exhibited outstanding PEC performance after modification with CdS and TiO$_2$. In particular, one-dimensional (1D) nanostructures (*i.e.*, nanowires, nanorods,

and nanotubes), especially vertically aligned ones, have been widely used to improve the PEC performance owing to the advantages of enhanced light trapping, short carrier diffusion length, and increased specific surface area compared with the bulk structures [26–29]. Therefore, 1D $CuInS_2$ nanoarrays are considered to eventually lead to the overall goal of high efficient and scalable PEC photocathodes.

Up to now, there are only a few reports on the synthesis of 1D $CuInS_2$ nanoarrays. Shi et al. [30] proposed a one-step solvothermal approach with porous alumina as the hard template for the fabrication of $CuInS_2$ nanowire arrays (NWAs). Wu et al. [31] demonstrated the synthesis of $CuInS_2$ nanotube arrays using a successive ionic layer absorption and reaction (SILAR) process with self-dissolved ZnO nanowire template. Sheng et al. [16] reported the preparation of $CuInS_2$ nanorod arrays *via* annealing Cu-In intermetallic compound precursor thin film under a H_2S and N_2 atmosphere. Nevertheless, it is challenging to fabricate high-quality $CuInS_2$ nanoarrays in large-scale by the above methods, and their PEC performance has not been investigated. Recently, Yang et al. [32] reported the fabrication of vertically aligned $CuInS_2$ nanorod arrays from an aqueous solution using anodic aluminum oxide (AAO) template-assisted growth and transfer. However, the fabrication procedures for both the $CuInS_2$ nanorod arrays and the corresponding photocathodes are very complicated, resulting in poor PEC performance (photocurrent density: ~2 μA/cm^2 at 0.3 V *vs.* RHE). Although there are previous studies for the preparation of $CuInS_2$/$CuInSe_2$ nanomaterials (nanocrystals [33], nanoplates [34,35], nanospheres [36], nanowire bundles [37], etc.) using CuxS/CuSe as the self-sacrificial template [38], their powder-like morphologies have limited their applications especially for PEC water splitting as photoelectrodes.

Herein, we first report the fabrication of $CuInS_2$ NWAs by a novel self-sacrificial template-directed method using Cu_2S NWAs as the template through a solvothermal process. The template-mediated growth mechanism has been proposed according to the experimental results. The PEC performance of the $CuInS_2$ NWAs was investigated compared to the pristine Cu_2S NWAs. Moreover, CdS quantum dots (QDs) were subsequently decorated onto the $CuInS_2$ nanowires to further improve the PEC activity.

2. Experimental

2.1. Synthesis of CuInS$_2$ NWAs

The pristine Cu_2S NWAs were grown on Cu mesh *via* a gas-solid reaction method (see Scheme 1a) [39–41]. The volume ratio of H_2S and O_2 was 2:1, and the reaction temperature was set to be 30 °C. After 10 h reaction, the Cu surface became black and fluffy (Fig. S1), dense Cu_2S NWAs were grown on the surface. The $CuInS_2$ NWAs were synthesized *via* solution transformation of Cu_2S NWAs in an autoclave by a solvothermal reaction (Scheme 1b–d). Typically, a Cu_2S NWAs substrate (2 cm × 2 cm) was put into a Teflon autoclave angle against the vessel wall, facing down, and 10 mL ethylene glycol solution containing 0.15 M InCl$_3$ and 0.3 M thioacetamide was poured into the autoclave to immerse the substrate. The autoclave was then put into an oven heating at 200 °C for a certain reaction time and cooled down to room temperature naturally.

2.2. Decoration of CdS QDs onto CuInS$_2$ NWAs

A SILAR method was used to deposit CdS QDs onto the $CuInS_2$ NWAs [42]. As shown in Scheme 1e–f, the $CuInS_2$ NWAs were immersed into the following solutions in sequence: 0.1 M Cd(NO$_3$)$_2$ ethanol solution for 20 s, deionized water for 10 s, 0.1 M Na$_2$S aqueous solution for 20 s, and then ethanol for 10 s. The four-step process

is called one SILAR cycle, and the thickness of the CdS layer can be controlled by the deposition cycle.

2.3. Characterization

The morphologies of the samples were characterized by a field emission scanning electron microscopy (FE-SEM, Carl Zeiss Ultra 55, Germany) operating at 20 kV. Transmission electron microscopy (TEM, JEM-2100, JEOL, Japan) operating at 200 kV was used to observe the microstructures of the samples. The crystalline structure was analysed by X-ray diffraction (XRD) using an advanced X-ray diffractometer (D8 ADVANCE, Bruker, Germany) in the diffraction angle range 2θ = 20–80°, with Cu Kα radiation (λ = 0.154056 nm) at voltage of 40 kV and a current of 40 mA. The Raman spectra were acquired by using a dispersive Raman microscope (Senterra R200-L, Bruker Optics, Germany), operated with a 532 nm laser. The X-ray photoelectron spectra (XPS) were acquired using a Japan Kratos Axis UltraDLD spectrometer with a monochromatic Al Kα source (1486.6 eV). The UV-vis-NIR absorption and diffuse reflectance spectra (DRS) were carried out using a UV-vis-NIR spectrophotometer (Lambda 950, PerkinElmer, USA). The photoluminescence (PL) spectra were obtained with a steady-state and time-resolved fluorescence spectrofluorometer (QM/TM/IM, PTI, USA).

2.4. PEC measurements

For easy measurement, the samples were fixed on glass slides by epoxy resin (see Scheme 1g), and an enamelled Cu wire was connected to the side part of the Cu substrate using conductive silver paint [43]. To prevent photocurrent leakage, the uncoated parts of the electrode were isolated with epoxy resin, and the exposed area for absorbing the light was ~1.0 cm^2. A three-electrode PEC cell using a 200 mL aqueous solution of 1.0 M KCl (pH = 5.97) was used to carry out the current density measurements.

The sample as working electrode (WE), Pt mesh as counter electrode (CE), and Ag/AgCl (saturated KCl) as reference electrode (RE) were the three electrodes in the PEC cell. Illumination was provided by a solar simulator (CHF-XM500, Beijing Perfectlight) using a 500 W Xenon lamp and equipped with AM 1.5 G filter. Light power intensity was maintained at 100 mW cm^{-2} at the sample position. An electrochemical workstation (CHI 650E) was used to measure current-voltage characteristics of the photocathodes under chopped light irradiation (light on/off cycle: 10 s), with a scan rate of 5 mV s^{-1}. The transient photocurrent densities were produced under chopped light irradiation (light on/off cycle: 10 s) at a fixed electrode potential of −0.55 V *vs.* Ag/AgCl (0 V *vs.* RHE).

The measured potentials *versus* the Ag/AgCl RE were converted to the RHE scale *via* the Nernst equation:

$$E_{RHE} = E_{Ag/AgCl} + 0.059\,pH + E_0 \tag{1}$$

where E_{RHE} is the converted potential *versus* RHE, $E_{Ag/AgCl}$ is the experimental potential measured against the Ag/AgCl RE, and E_0 is the standard potential of Ag/AgCl (saturated KCl) at 25 °C (*i.e.,* 0.197).

The electrochemical impedance spectra (EIS) was carried out with a sinusoidal perturbation with 5 mV amplitude and frequencies ranging from 100 kHz to 0.1 Hz. The EIS measurement for the Mott-Schottky plot was performed at frequency of 1 kHz with AC amplitude of 10 mV and scan step of 1 mV.

The incident photon to current efficiency (IPCE) was carried out at 0 V *vs.* RHE under monochromatic irradiation from the Xenon lamp equipped with bandpass filters to show the spectral distribution of photocurrent generation. The IPCE is expressed as:

$$IPCE = (1240I)/(\lambda P_{light}) \tag{2}$$
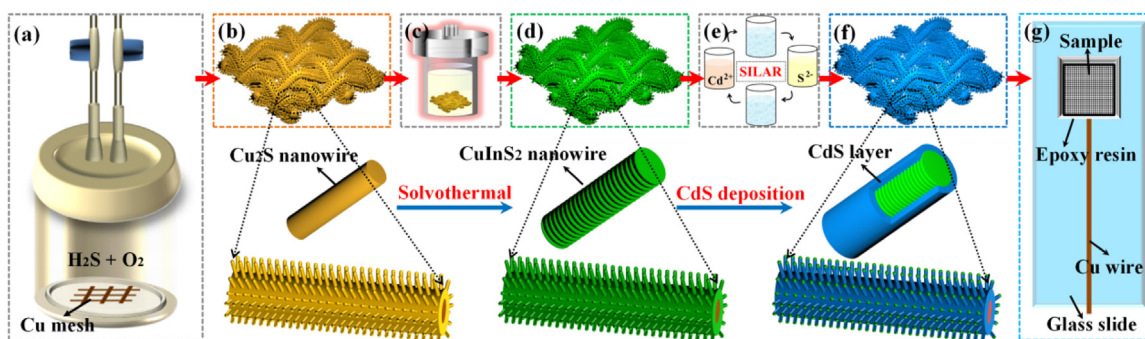
Scheme 1. Photocathode design and synthesis strategy of CuInS$_2$-based NWAs: (a) Gas-solid reaction for the growth of Cu$_2$S NWAs, (b–d) Solution transformation of Cu$_2$S into CuInS$_2$ NWAs, (e–f) SILAR deposition of CdS QDs onto the CuInS$_2$ NWAs, (g) Schematic illustration of the photocathode design.

where I is the photocurrent density (mA cm^{-2}), λ is the incident light wavelength (nm), and P$_{light}$ (mW cm^{-2}) is the power density of monochromatic light at a specific wavelength.

3. Results and discussion

Fig. 1 shows the SEM images of the NWAs obtained with different solvothermal reaction times. It can be seen that after solvothermal reaction the diameters of the nanowires are increased from ∼350 nm to ∼550 nm and their surfaces become rougher, indicating the reaction between Cu$_2$S and In^{3+}. XRD was used to characterize the transformation of Cu$_2$S into CuInS$_2$ (Fig. 2a). After only 1 h reaction, the peaks of Cu$_2$S (JCPDS card No. 33-0490) become very weak [43], while three dominant peaks emerge at 28, 47, and 55°corresponding to the (112), (220), and (132) planes of the chalcopyrite (tetragonal) structured CuInS$_2$ (JCPDS card No. 47-1372), respectively [25,44]. Meanwhile, two impurity phases for In$_2$S$_3$ exist at 27° and 30.2° (JCPDS card No. 33-0624). Further increasing the reaction time to 2 h, the weak peaks of Cu$_2$S have nearly disappeared and the intensity of the In$_2$S$_3$ impurity peaks is relatively decreased. As shown in Fig. 2b, Raman spectroscopy was used to obtain further insight into phase identification of the CuInS$_2$ nanostructures. Two strong peaks at 294, 305 cm^{-1} and a relatively weak peak at 340 cm^{-1} for CuInS$_2$ can be observed, which is consistent with the reported Raman study for CuInS$_2$ nanowires [30,32]. Additionally, a weak peak at 323 cm^{-1} can be assigned to the In$_2$S$_3$ impurity, and no other Raman peaks related to CuxS can be observed. The above results suggest that CuInS$_2$ NWAs can be prepared via solvothermal transformation of Cu$_2$S nanowire self-sacrificial template. The existence of In$_2$S$_3$ impurities may result from the formation of In$_2$S$_3$ microparticles in the reaction solution (see Fig. S2), which can easily adhere to the CuInS$_2$ NWAs in the solvothermal reaction process, as pointed out in the circular regions in Fig. 1b$_1$,c$_1$. Fortunately, In$_2$S$_3$ was reported to be an efficient *n*-type surface modifier for improving the PEC properties of CuInS$_2$-based photocathodes [14,45].

TEM was used to further characterize the microstructures of the CuInS$_2$ nanowires. As shown in Fig. 3a, b, the CuInS$_2$ nanowires exhibit irregular screw-like morphologies. The corresponding selected area electron diffraction (SAED) pattern (inset, Fig. 3b) reveal the polycrystalline structure of the CuInS$_2$ nanowire. It can be inferred that a CuInS$_2$ nanowire is constructed by many stacked nanoplates. The high-magnification TEM image for the edge of a representative CuInS$_2$ nanoplate (Fig. 3c) demonstrates its high crystallinity, and the fringe spacing of 0.32 nm in the high-resolution TEM (HRTEM) image (inset, Fig. 3c) matches well with the interplanar spacing of the {112} planes of CuInS$_2$. The results indicate that the CuInS$_2$ nanoplates are oriented along the direction of [221], which is parallel to the axial direction of CuInS$_2$ nanowire. The above analysis is also supported by the XRD results, where the

peak intensity of (112) plane is much higher than that of the other two planes. Furthermore, energy-dispersive X-ray spectroscopy (EDX) was used to analyse the composition of the as-synthesized CuInS$_2$ nanowires, and the results suggest that the ratio of Cu:In:S is 1:0.8:1.8 (Fig. S3). The expression of (Cu + 3In)/2S is smaller than unity, indicating that the Cu-rich CuInS$_2$ nanowires should behave as a *p*-type semiconductor [31]. Additionally, the composition distribution of the CuInS$_2$ nanowires was also characterized by the EDX mapping as shown in Fig. 3d–f. The Cu, In, S element signals are distributed homogeneously through the nanowire, further confirming the complete transformation of Cu$_2$S into CuInS$_2$.

To further confirm the composition and valence states of the as-obtained CuInS$_2$ nanowires, XPS analysis was performed. The survey XPS spectrum (Fig. S4) indicates that all the Cu, In, and S elements exist on the surfaces of CuInS$_2$ nanowires. The Cu 2p, In 3d, and S2p core levels were also studied in detail. As shown in Fig. 3g, the binding energies of Cu 2p$_{1/2}$ and Cu 2p$_{3/2}$ are centred at 951.6 eV and 931.8 eV, which is in good agreement with the reported values in previous literature. There is no satellite peak related with Cu^{2+} between the Cu 2p$_{1/2}$ and Cu 2p$_{3/2}$, proving the absence of Cu^{2+} [46]. The In 3d signal shown in Fig. 3h displays two peaks at 452.1 eV and 444.6 eV, corresponding to the characteristic In 3d$_{3/2}$ and In 3d$_{5/2}$, respectively [47]. As shown in Fig. 3i, the S 2p core splits into two obvious peaks at 162.6 eV and 161.3 eV, which can be assigned to the S 2p$_{1/2}$ and S 2p$_{3/2}$ due to the different binding with In and Cu, respectively [47]. According to the XPS measurements, the observed binding energies of Cu 2p, In 3d, and S 2p core levels for CuInS$_2$ NWAs are in good accordance with those reported [48,49].

We have also investigated the influence of In^{3+} concentration on the transformation of Cu$_2$S into CuInS$_2$. As shown in Fig. S5a, nanoplates with sizes of ∼100 nm form on nanowires at the lower In^{3+} concentration of 0.05 M. When the concentration is increased to 0.10 M, they are replaced by nanoparticles (Fig. S5b). Further increasing the In^{3+} concentration to as high as 0.15 M, nanowires with relatively smooth surfaces can be prepared (Fig. S5c). The corresponding XRD patterns (Fig. S6) indicate relatively higher proportion of In$_2$S$_3$ exist on CuInS$_2$ nanowires at lower In^{3+} concentration. The above results indicate that relatively higher In^{3+} concentration is beneficial to the insertion of In^{3+} into Cu$_2$S to form CuInS$_2$ with keeping the nanowire morphology unchanged.

To investigate the formation mechanism of the CuInS$_2$ nanowires, TEM characterization of the pristine Cu$_2$S nanowires and the nanowires obtained after 0.5 h solvothermal reaction was also conducted. As shown in Fig. 4a, b, the growth direction of the Cu$_2$S nanowires is perpendicular to the ($\bar{2}$04) plane, *i.e.*, the *c*-axis. From the HRTEM image shown in Fig. 4c, it can be clearly seen that the Cu$_2$S core is covered by a thin amorphous CuxO shell layer with thickness of ∼5 nm, which is confirmed by Raman analysis (Fig. S7). The result is the same as the Cu$_2$S nanowires prepared by the same
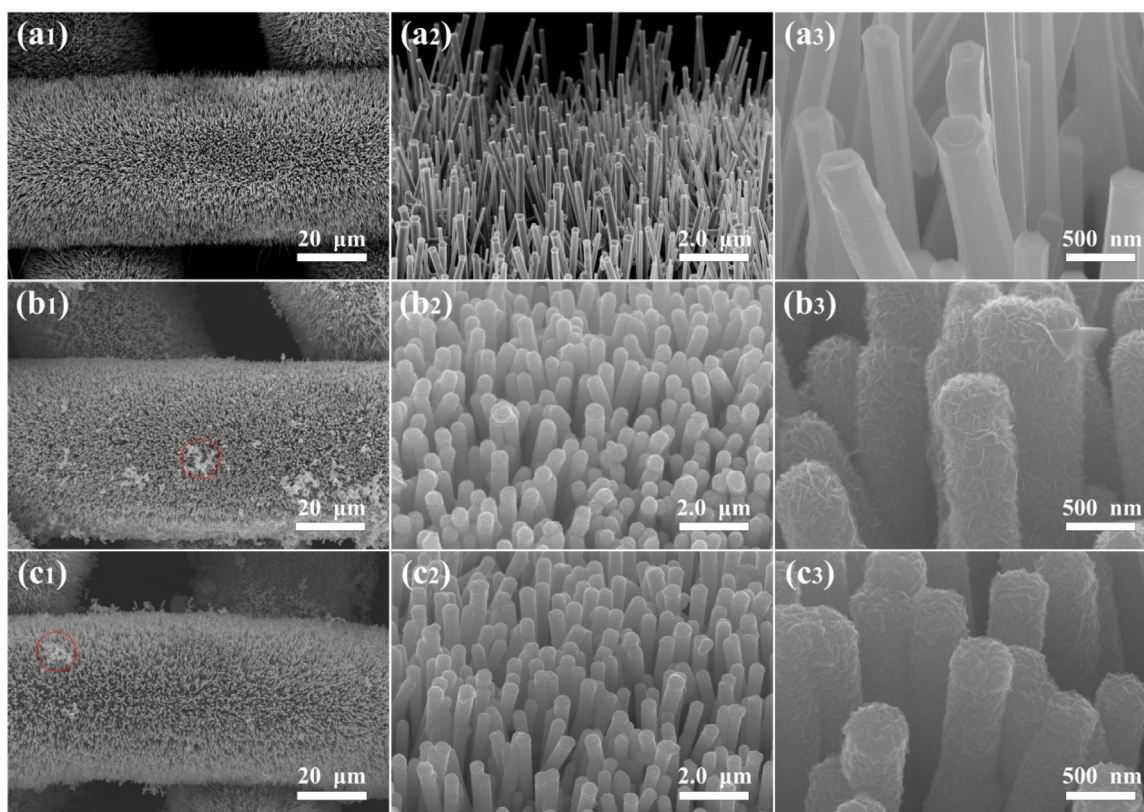
Fig. 1. SEM images of the NWAs obtained with different reaction times: (a_1–a_3) 0 h, (b_1–b_3) 1 h, and (c_1–c_3) 2 h.
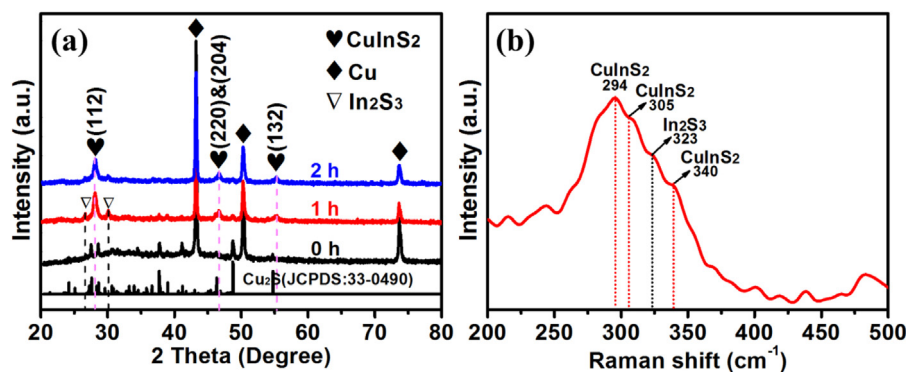

Fig. 2. (a) XRD pattern of the NWAs obtained with different reaction times. (b) Raman spectrum of the as-synthesized CuInS$_2$ NWAs.

method [39–41]. After 0.5 h solvothermal reaction, the nanowires have been eroded and exhibit irregular screw-like morphology, as shown in Fig. 4d. Further high-magnification TEM characterization (Fig. 4e, f) suggests that the erosion process proceeds preferentially along the direction perpendicular to the axial direction of nanowire, *i.e.*, the growth direction of the pristine Cu$_2$S nanowires (*c*-axis).

Based on the above results, a novel exchange-erosion formation mechanism is proposed to illustrate the formation of the screw-like CuInS$_2$ NWAs, as illustrated in Scheme 2a. During the solvothermal process, H$_2$S will be released *via* the reaction between thioacetamide and water in the heated solution, which then decomposes and provides H$^+$ and S^{2-} ions [25]. As the screw direction of the as-synthesized CuInS$_2$ nanowires is parallel to the *c*-axis of the pristine Cu$_2$S nanowires (see Fig. 3 and Fig. 4), it can be inferred that Cu$_2$S nanowires are firstly eroded by the H$^+$ ions preferentially along the ($\bar{2}$04) facets of Cu$_2$S [25], which can be ascribed to the alternated Cu and S layers structure along *c*-axis of Cu$_2$S as shown in Scheme 2b

[18,50]. Meanwhile, the In^{3+} ions in solution will also diffuse inward preferentially along the ($\bar{2}$04) facets of Cu$_2$S and exchange with the Cu$^+$ ions diffusing outward to form CuInS$_2$ in situ [18,33]. So relatively higher In^{3+} concentration is beneficial to this process (Fig. S5). Meanwhile, the released Cu$^+$ ions can also react with In^{3+} and S^{2-} in the solution, leading to the growth of CuInS$_2$ (Fig. 4f) [18]. Benefiting from the small discrepancy (~5.9%) between the interplanar spacing for the {$\bar{2}$04} planes of Cu$_2$S nanowire (0.34 nm) and that for the {112} planes of CuInS$_2$ (0.32 nm) as well as the similar alternated metal and S layers structure along the *c*-axis for Cu$_2$S and the [221] direction for CuInS$_2$, the ($\bar{2}$04) facets of Cu$_2$S nanowires are in favour of the growth of CuInS$_2$ with exposed (112) facets (see Scheme 2b, c).

The light absorption performance of the screw-like CuInS$_2$ NWAs has been investigated. As shown in Fig. 5, the CuInS$_2$ NWAs exhibit greatly enhanced light trapping ability compared to the pristine Cu$_2$S NWAs, especially in the long wavelength region. The
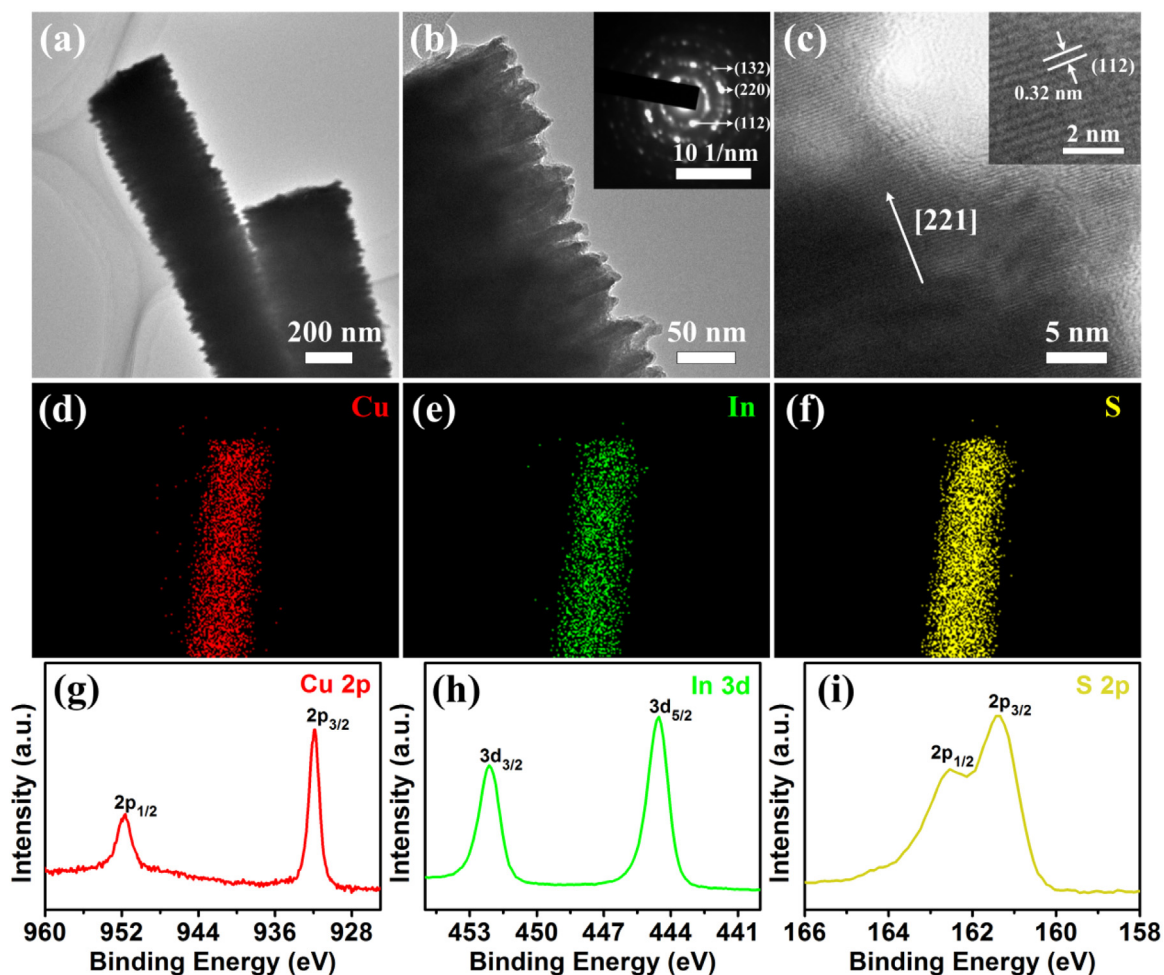
Fig. 3. (a, b) TEM images of CuInS$_2$ nanowires at different magnifications, inset: SAED pattern acquired from the edge of the CuInS$_2$ nanowire. (c) High-magnification TEM image of the edge of a CuInS$_2$ nanowire, inset: the representative HRTEM image. (d-f) Element mapping of Cu, In, and S, respectively, for a CuInS$_2$ nanowire. (g-i) XPS spectra of Cu 2p, In 3d, and S 2p, respectively, for the CuInS$_2$ NWAs.
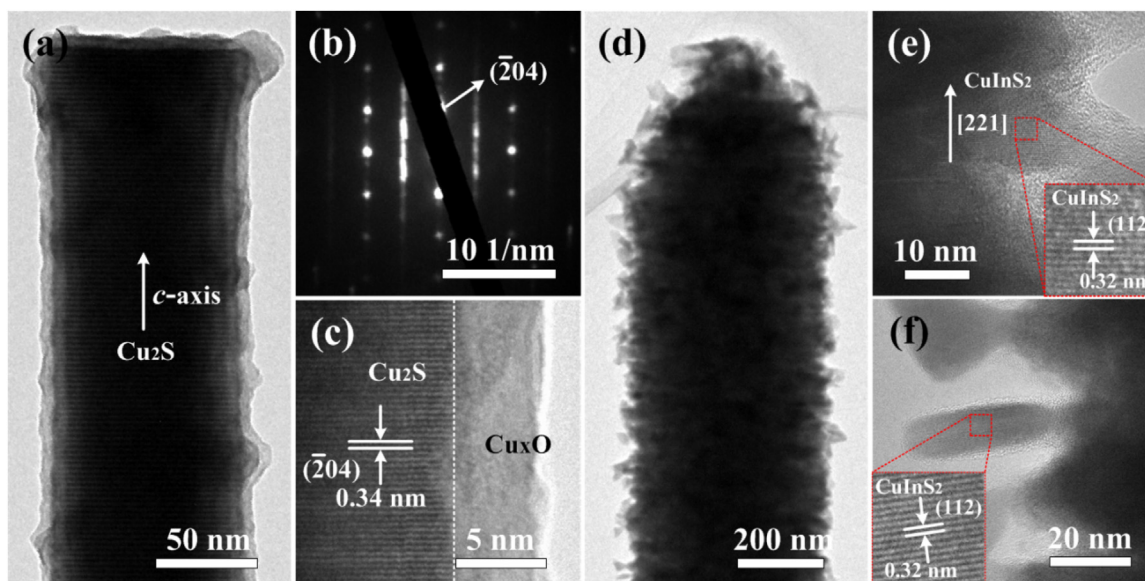

Fig. 4. TEM characterization of the pristine Cu$_2$S nanowire and the CuInS$_2$ nanowire obtained with the reaction time of 0.5 h: (a) TEM image of a pristine Cu$_2$S nanowire, (b) SAED pattern acquired from the top of the Cu$_2$S nanowire, (c) HRTEM image of the edge of the Cu$_2$S nanowire, (d) TEM image of a CuInS$_2$ nanowire, (e, f) different high-magnification TEM images of the edge of the CuInS$_2$ nanowire, inset: the representative HRTEM image.
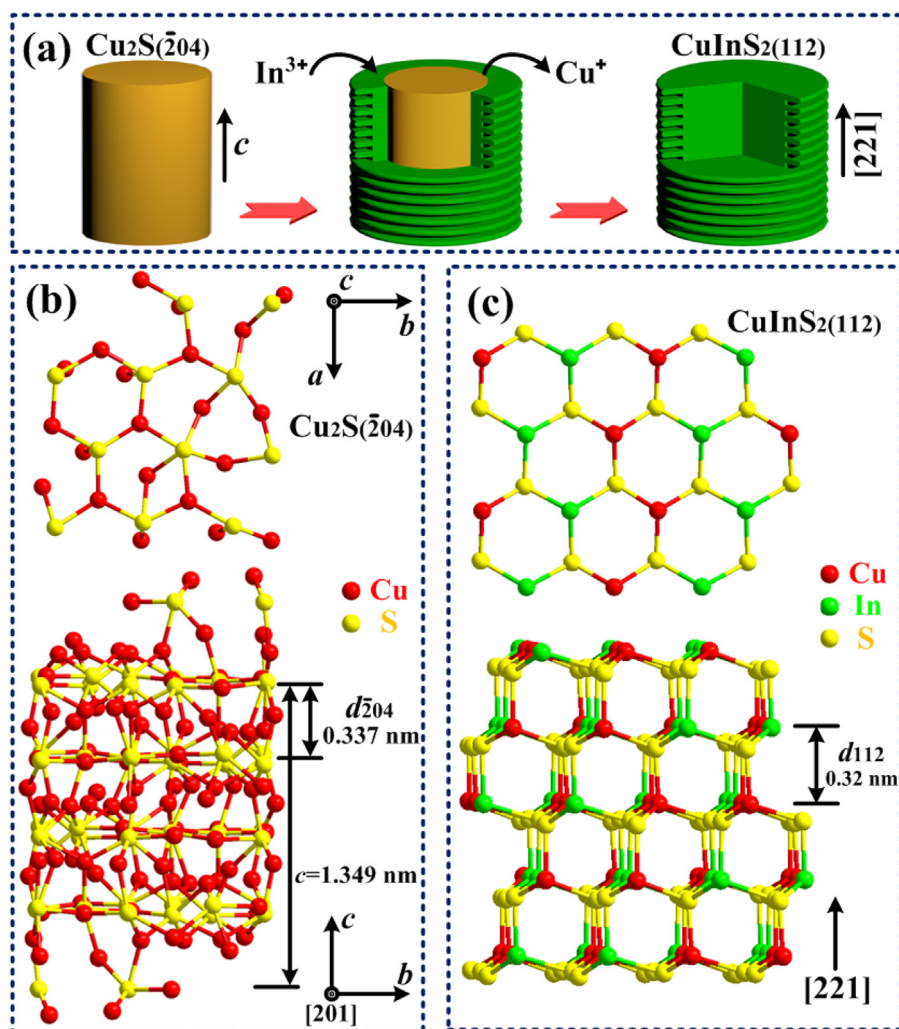
Scheme 2. (a) Schematic illustration for the formation of screw-like CuInS$_2$ nanowire. (b, c) Structural models of Cu$_2$S and CuInS$_2$, respectively.
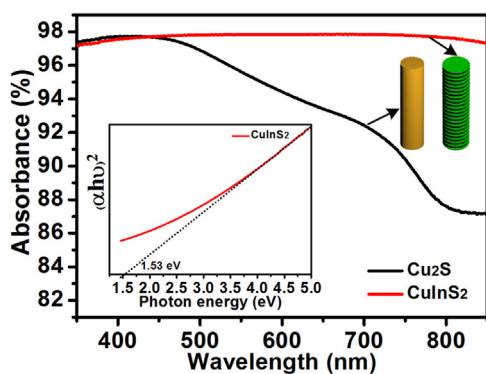

Fig. 5. UV–vis absorption spectra of the CuInS$_2$ and the pristine Cu$_2$S NWAs. Inset: energy band gap determination of the CuInS$_2$ NWAs.

absorbance of the Cu$_2$S NWAs gradually decreases from 97.4% at 350 nm to 87.2% at 850 nm with the increase of wavelength. Nevertheless, the CuInS$_2$ NWAs show the absorbance of 97.2-97.9% over the whole wavelength range of 350–850 nm. The greatly improved absorbance can be attributed to the optimized bandgap (1.25 eV for Cu$_2$S, see Fig. S8, and 1.53 eV for CuInS$_2$, inset of Fig. 5) as well as the rough screw-like morphology for light trapping.

To obtain efficient photocathodes, CuInS$_2$/CdS core/shell NWAs have been fabricated *via* decorating CdS QDs onto the surfaces

of CuInS$_2$ nanowires using a facile SILAR method. The deposition cycle time was used to control the thickness of the CdS layer, and the CuInS$_2$/CdS-x NWAs were obtained, where x represents the deposition cycle of CdS. The EDX of the CuInS$_2$/CdS-10 NWAs (Fig. S9) reveals that the core/shell nanowires are composed of Cu, In, Cd, and S elements, suggesting that CdS QDs can be successfully loaded on the surfaces of CuInS$_2$ nanowires by this method. The SEM images of the CuInS$_2$/CdS-10 NWAs (Fig. 6a–c) show the uniform growth of CdS shell layer, which is confirmed by the low-magnification TEM image of a typical CuInS$_2$/CdS-10 core/shell nanowire shown in Fig. 6d, where the measured diameter of the CuInS$_2$ core is ∼655 nm and the thickness of the CdS shell is ∼75 nm. Fig. 6e is the high-magnification TEM image of the edge for the CuInS$_2$/CdS-10 core/shell nanowire, in which the CdS QDs with sizes of about several nanometres can be observed. The fringe spacing of 0.34 nm in the representative HRTEM image (inset, Fig. 6e) corresponds to the (111) planes of CdS [42]. The corresponding selected area electron diffraction (SAED) pattern (Fig. 6f) reveals the polycrystalline nature of the CdS layer. Additionally, the EDX mapping of a CuInS$_2$/CdS-10 nanowire (Fig. 6g–j) was used to further testify the uniform distribution of CdS QDs on the whole surfaces of CuInS$_2$ nanowire.

The PEC measurements were carried out using a three-electrode configuration with NWAs, Ag/AgCl electrode, and Pt mesh as the WE, RE, and CE, respectively, in an aqueous solution containing 1.0 M KCl (pH = 5.97). Fig. 7a shows the linear sweep voltamme-
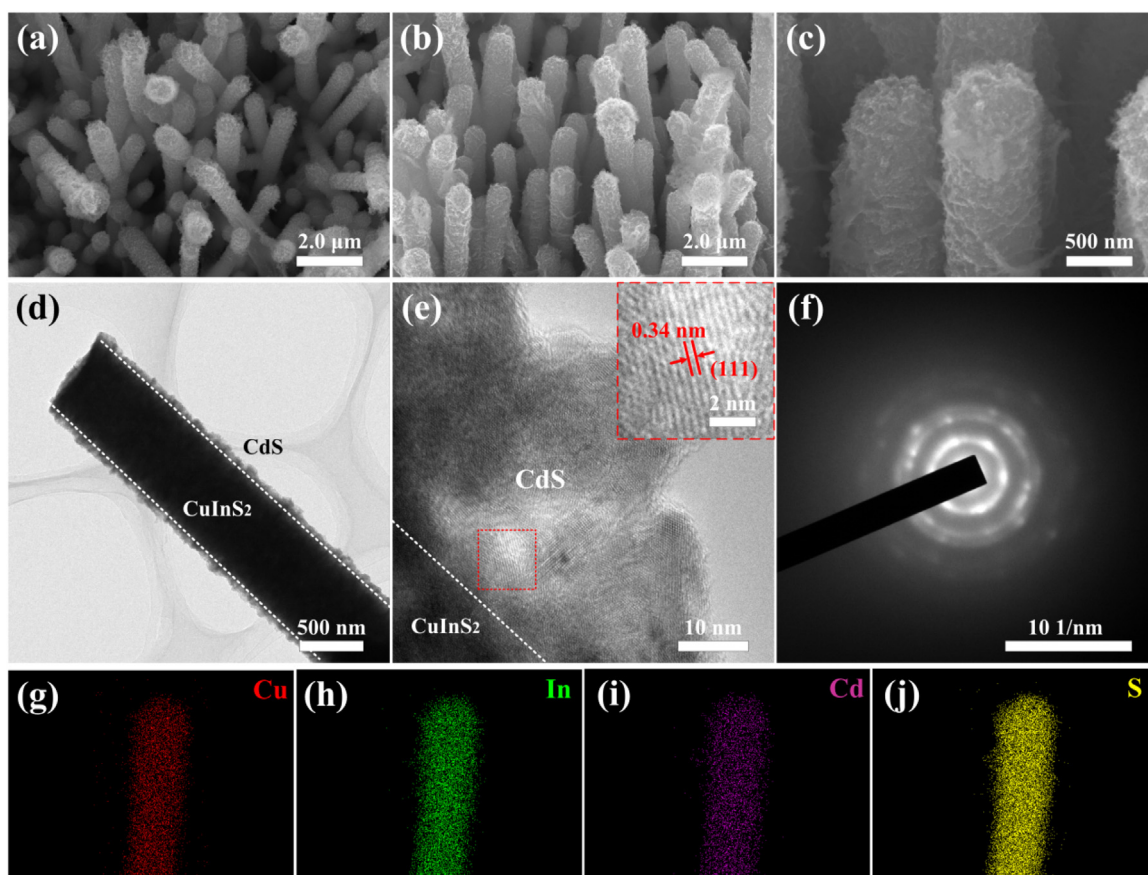
Fig. 6. (a–c) SEM images of the CuInS$_2$/CdS-10 NWAs. (d) Low-magnification TEM image of a CuInS$_2$/CdS-10 nanowire. (e) High-magnification TEM image of the edge of the CuInS$_2$/CdS-10 nanowire, inset: the representative HRTEM image of a CdS QD. (f) SAED pattern acquired from the edge of the CuInS$_2$/CdS-10 nanowire. (g–j) Element mapping of Cu, In, Cd and S, respectively, for a CuInS$_2$/CdS-10 nanowire.

try (LSV) curves under chopped white light illumination (AM 1.5G, 100 mW cm^{-2}) for the CuInS$_2$ and the pristine Cu$_2$S NWAs. The photocurrent of the CuInS$_2$ NWAs decreases with the positive scanning of the applied bias, indicating a standard *p*-type feature of CuInS$_2$, which is consistent with the previous EDX analysis. Furthermore, the CuInS$_2$ photocathode exhibits greatly enhanced photocurrent compared to the pristine Cu$_2$S NWAs, and the absolute photocurrent of the CuInS$_2$ and Cu$_2$S NWAs at −0.1 V *vs.* RHE are 0.14 and 0.3 mA cm^{-2}, respectively. Fig. 7b illustrates the transient current density under chopped illumination for the corresponding samples at 0 V *vs.* RHE, exhibiting good switching behaviour of both the Cu$_2$S and CuInS$_2$ NWAs photocathodes. It is also obvious that the photocurrent of CuInS$_2$ NWAs is much higher than that of the pristine Cu$_2$S NWAs. There are two possible reasons for the enhanced photocurrent: One is that the CuInS$_2$ NWAs exhibit optimized bandgap for increased light absorption compared to the Cu$_2$S NWAs (see Fig. 5). The other one is that the screw-like morphology for CuInS$_2$ nanowires can provide increased contact area for fast interfacial photocarrier separation and PEC reactions [51]. Additionally, the PEC performance of the CuInS$_2$ NWAs is much higher than that of the vertically aligned CuInS$_2$ nanorod arrays fabricated by AAO template-assisted method ($\sim$2 µA/cm^2 at 0.3 V *vs.* RHE) [32]. This can be due to the high crystallinity of the CuInS$_2$ nanowires derived from the single-crystal Cu$_2$S nanowire template, as well as the good adhesiveness between nanowires and Cu substrate.

The PEC performance of the CuInS$_2$ NWAs photocathodes can be further improved by modification with CdS QDs. From the LSV curves of the CuInS$_2$/CdS-x NWAs under chopped illumination (Fig. 7c), obvious photocurrent enhancement can be observed for

the samples decorated with CdS QDs. It is found that the photocurrent of CuInS$_2$/CdS-x NWAs at −0.1 V *vs.* RHE (Fig. S10) firstly increases along with the increase of the deposition cycle of CdS, and reaches a maximum for the CuInS$_2$/CdS-10 NWAs showing the optimal photocurrent of 0.71 mA cm^{-2}. However, the measured photocurrent of CuInS$_2$/CdS NWAs decreases with further elongation of the deposition cycle as charge transfer will be hindered by a dense packing of CdS QDs [52]. Fig. 7d shows the I-t curves of the CuInS$_2$/CdS-x NWAs at 0 V *vs.* RHE under chopped illumination, which also demonstrate the enhanced PEC activity as well as the good switching behaviour of the samples.

Fig. 7e displays the EIS of the CuInS$_2$ and the CuInS$_2$/CdS-10 NWAs at dark and under illumination. It can be seen that all Nyquist plots display a semicircle at high frequencies whose diameter represents the charge transfer resistance (R_{ct}), which controls the electron transfer kinetics of the redox probe at the electrode interface [8]. The inset of Fig. 7e depicts the corresponding equivalent circuit, where R_s denotes the bulk resistance, originating from the electrolyte and the electrode, *CPE* is the constant phase element that models capacitance of the double layer, and *W* stands for the Warburg impedance originated from the diffusion process at the electrode surface. The fitting results of R_{ct} for the CuInS$_2$/CdS-10 NWAs in the dark and under illumination are 1784 and 965 Ω cm^2, respectively, which are smaller than the corresponding values of the bare CuInS$_2$ NWAs (2437 and 1538 Ω cm^2, respectively). The results suggest that decoration of CdS QDs can facilitate electron transfer from CuInS$_2$ nanowires to electrolyte due to the formation of *p-n* junction, then resulting in enhanced PEC performance [25].
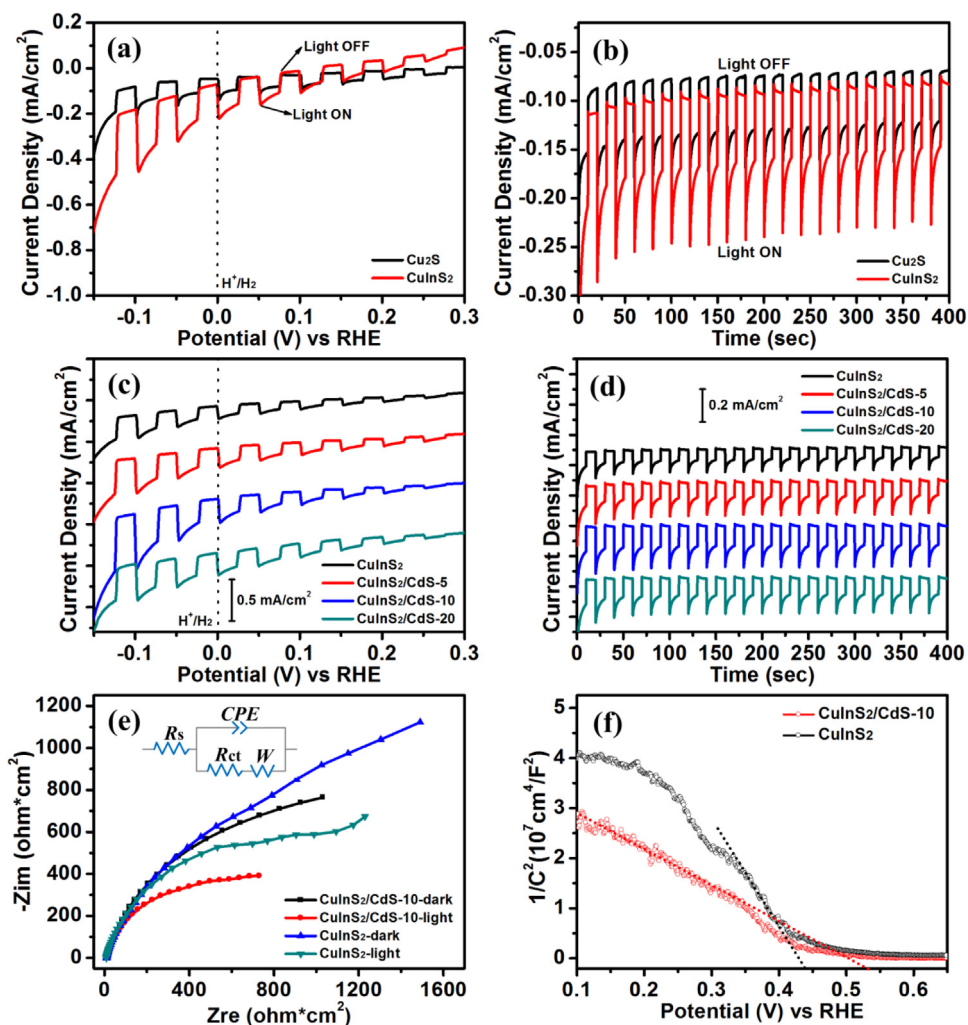
Fig. 7. (a) LSV curves of the $CuInS_2$ and the pristine Cu_2S NWAs under chopped illumination. (b) Amperometric I-t curves of the $CuInS_2$ and the pristine Cu_2S NWAs at 0 V *vs.* RHE under chopped illumination. (c) LSV curves of the $CuInS_2/CdS$-x NWAs under chopped illumination. (d) Amperometric I-t curves of the $CuInS_2/CdS$-x NWAs at 0 V *vs.* RHE under chopped illumination. (e) Nyquist plots of the $CuInS_2$ and $CuInS_2/CdS$-10 NWAs at dark and under illumination. (f) Mott-Schottky plots of $CuInS_2$ and $CuInS_2/CdS$-10 NWAs.
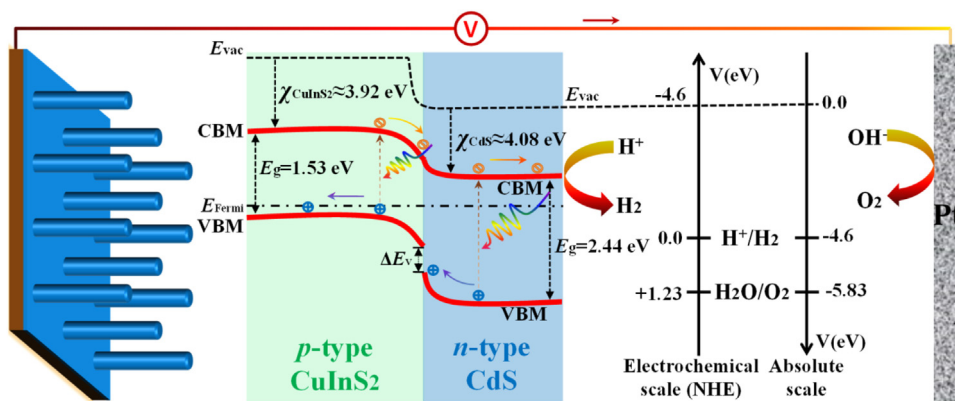
Scheme 3. Energy band diagram of the $CuInS_2/CdS$ heterojunction for PEC water splitting.

The formation of *p–n* junction will also lead to cathodic polarization, which then thickens the depletion layer [10]. As a result, the flat-band potential (E_{FB}) will shift positively. Constructing a Mott-Schottky plot is a typical plot of determining E_{FB}. Fig. 7f shows the Mott-Schottky plots of $CuInS_2$ and $CuInS_2/CdS$-10 NWAs, in which $1/C^2$ is plotted against potential. The negative slope of the plots also

demonstrates the *p*-type property of the $CuInS_2$ nanowire arrays, as confirmed by the EDX analysis and the observed photocurrent behaviour. The E_{FB} can be estimated from the x-intercept of the linear extrapolation of the linear region. The results suggest that the bare $CuInS_2$ NWAs have an E_{FB} of 0.44 V *vs.* RHE, while E_{FB} shifts positively to 0.53 V after surface decoration with CdS QDs. This indi-
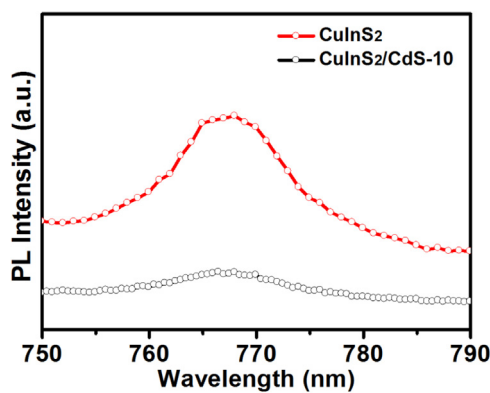
Fig. 8. Room-temperature PL spectra of $CuInS_2$ and $CuInS_2/CdS$-10 NWAs, excited at 587 nm.
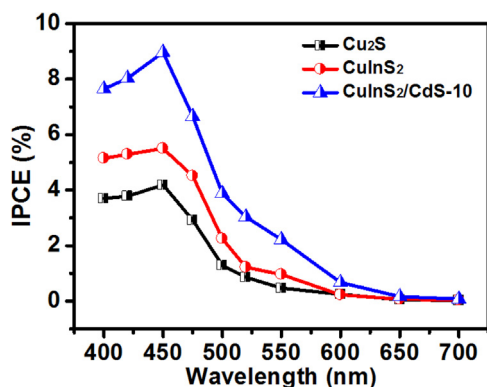

Fig. 10. Photocurrent density decay at 0 V *vs.* RHE for the $CuInS_2/CdS$-10 NWAs photocathode under continuous AM 1.5 G irradiation, inset: the magnification of the change in photocurrent for this electrode between 290 and 350s.

Fig. 9. IPCE spectra of the pristine Cu_2S, $CuInS_2$, and $CuInS_2/CdS$-10 NWAs at 0 V *vs.* RHE.

cates that CdS QDs decoration lowers the $CuInS_2$ energy bands, in turn facilitating charge separation at more anodic potentials, which is favourable for low onset potentials [32].

The recombination and transfer behaviour of the photo-generated electrons and holes in the heterojunction is further verified by PL. Fig. 8 shows the room-temperature PL spectra of $CuInS_2$ and $CuInS_2/CdS$-10 NWAs. The spectrum of bare $CuInS_2$ NWAs exhibit a broad emission at 768 nm corresponding to a peak energy of 1.61 eV, which is attributed to near-band-edge emission. The emission peak of $CuInS_2$ nanowires is close to that previously reported for the $CuInS_2$ nanoparticles (1.68 eV) [53]. After the modification of CdS QDs, the PL intensity of $CuInS_2$ NWAs is significantly deceased. This quenching behaviour confirms the excited-state interaction between the two semiconductors and demonstrates deactivation of the excited $CuInS_2$ nanowires *via* electron transfer to the CdS layers. That is to say, the photo-generated electrons and holes can be separated more efficiently in the $CuInS_2/CdS$ heterostructure. This result matches well with the EIS and E_{FB} analysis, and also proves the enhanced PEC performance by CdS QDs decoration.

As shown in Fig. 9, the IPCE measurement was carried out at 0 V *vs.* RHE to further evaluate the improved PEC performance of the $CuInS_2$ NWAs-based photocathodes. It can be seen that both the pristine Cu_2S NWAs and the $CuInS_2$ NWAs-based photocathodes show relatively higher IPCE in the short wavelength region, and exhibit the optimal value at the incident wavelength of about 450 nm. Compared to the pristine Cu_2S NWAs, the $CuInS_2$ NWAs show substantially enhanced IPCE, especially in the short wavelength region. It shows an optimal IPCE of 5.5%, which is much higher than that of the pristine Cu_2S NWAs (4.2%). Besides, the IPCE of $CuInS_2$ NWAs has been further enhanced by the decoration of CdS
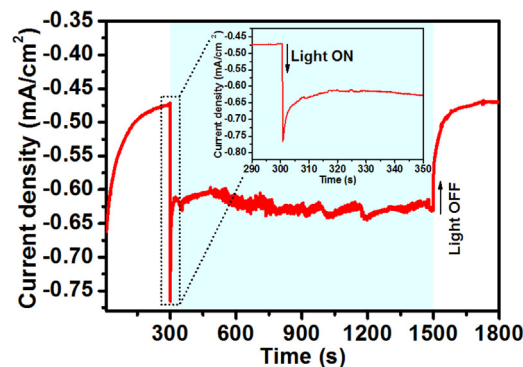
QDs, and the $CuInS_2/CdS$-10 NWAs has realized an IPCE as high as 9.0%.

As shown in Fig. 10, the stability of the $CuInS_2/CdS$-10 NWAs photocathodes was evaluated with chronoamperometric measurements at 0 V *vs.* RHE under continuous AM 1.5G irradiation over 20 min, a condition which is widely used as a semi-standard for comparing photo stability of a semiconductor [8,54,55]. When the light was turned on (inset, Fig. 10), a transient photocurrent density of 0.30 mA/cm² was observed, which then dramatically decreased to a relatively stable value of 0.14 mA/cm² in 20 s. The photocathode current overshoots in the beginning of switching light on can be ascribed to the accumulation of photo-generated carriers at the interfaces between nanowires and electrolyte [56]. During the continuous irradiation over 20 min, fluctuating current could be clearly seen. Additionally, as the light was turned off, it was a long time for the current to recover to the position close to the original dark current. These can be attributed to the photocorrosion of the photocathodes as both $CuInS_2$ and CdS are not good photocorrosion-resistant material. Luo et al. [25] reported that the modification of aluminium-doped zinc oxide and titanium dioxide protecting layers on the $CuInS_2/CdS$ heterojunction nanostructured films by atomic layer deposition method can greatly improve the photocurrent as well as the stability of the photocathodes. It is believed that both the photocurrent and stability of the $CuInS_2/CdS$ NWAs photocathode can be further improved by the modification of these oxide protecting layers.

Scheme 3 is the idealized energy band diagram of the $CuInS_2/CdS$ heterojunction illustrating the PEC water splitting mechanism and charge transfer process in the $CuInS_2/CdS$ NWAs photocathode [11]. According to the literature, the hydrogen reduction potential $\mu_e^{H+/H2}$ can be chosen to be equal to -4.6 eV corresponding to the redox potential of the normal hydrogen electrode (NHE) [57]. As both the conduction band minimum (CBM) and valence band maximum (VBM) of $CuInS_2$ are higher than those of CdS, a type-II heterostructure of $CuInS_2/CdS$ can promote the separation of the photo-generated carriers [11,25]. Additionally, this ideal band structure of the $CuInS_2/CdS$ core/shell nanowire is suitable for improving the photocurrent generation of PEC cells because the CBM of $CuInS_2$ (-3.92 eV) is higher than the $\mu_e^{H+/H2}$ and the VBM of CdS (-6.52 eV) lower than the $\mu_e^{H2O/O2}$ (-5.83 eV) [11]. Upon PEC water splitting, photo-excited electrons move towards the CdS-electrolyte interface to induce the reaction $2H_2O + 2e^- \rightarrow H_2 + 2OH^-$. A majority of holes move towards the back contact and through the outer circuit to the counter electrode where oxygen evolves.

4. Conclusion

In conclusion, the screw-like $CuInS_2$ NWAs have successfully synthesized using Cu_2S NWAs as self-template, which show diameters of 400–700 nm and lengths of several micrometres. It is observed that they are constructed by many stacked nanoplates oriented along the direction of [221]. The experimental results suggest that the key point for the formation of screw-like $CuInS_2$ nanowires is the In^{3+} insertion preferentially along the $(\bar{2}04)$ facets of Cu_2S nanowires probably due to the unique alternated Cu and S layers structure along the c-axis of the pristine Cu_2S nanowires. It is found that this cation-exchange process is greatly influenced by the In^{3+} concentration in the reaction solution, and relatively higher concentration is in favour of the formation of $CuInS_2$ with inheriting the nanowire morphology of the pristine Cu_2S template. The $CuInS_2$ NWAs have exhibited greatly enhanced PEC performance compared to the pristine Cu_2S NWAs due to the enhanced light absorption as well as their screw-like surfaces for increased specific surface area. The $CuInS_2/CdS$ NWAs have demonstrated an optimal photocurrent of $0.71 \, mA \, cm^{-2}$ and an IPCE of 9.0% at 450 nm. Though here only the transformation of Cu_2S into $CuInS_2$ is demonstrated, there is no barrier to generalize the method to other copper chalcopyrite-based NWAs, which may show numerous applications in photovoltaic and optoelectronic devices.

Acknowledgements

Appendix A. Supplementary data

Supplementary data associated with this article can be found, in the online version, at http://dx.doi.org/10.1016/j.apcatb.2016.10.051.

References

[1] T. Hisatomi, J. Kubota, K. Domen, Chem. Soc. Rev. 43 (2014) 7520–7535.
[2] M. Grätzel, Nature 414 (2001) 338–344.
[3] A. Fujishima, K. Honda, Nature 238 (1972) 37–38.
[4] J. Gan, X. Lu, Y. Tong, Nanoscale 6 (2014) 7142–7164.
[5] M.G. Walter, E.L. Warren, J.R. McKone, S.W. Boettcher, Q. Mi, E.A. Santori, N.S. Lewis, Chem. Rev. 110 (2010) 6446–6473.
[6] Y. Wang, Q. Wang, X. Zhan, F. Wang, M. Safdar, J. He, Nanoscale 5 (2013) 8326–8339.
[7] F.E. Osterloh, Chem. Soc. Rev. 42 (2013) 2294–2320.
[8] Z. Zhang, R. Dua, L. Zhang, H. Zhu, H. Zhang, P. Wang, ACS Nano 7 (2013) 1709–1717.
[9] P. Sheng, W. Li, X. Tong, X. Wang, Q. Cai, J. Mater. Chem. A 2 (2014) 18974–18987.
[10] M. Moriya, T. Minegishi, H. Kumagai, M. Katayama, J. Kubota, K. Domen, J. Am. Chem. Soc. 135 (2013) 3733–3735.
[11] Y. Choi, M. Beak, K. Yong, Nanoscale 6 (2014) 8914–8918.
[12] H. Kaga, Y. Tsutsui, A. Nagane, A. Iwase, A. Kudo, J. Mater. Chem. A 3 (2015) 21815–21823.
[13] T.J. Jacobsson, C.P. Björkman, M. Edoff, T. Edvinsson, Int. J. Hydrogen Energy 38 (2013) 15027–15035.
[14] W. Gunawan, S. Septina, T. Ikeda, T. Harada, K. Minegishi, M. Domen, M. Matsumura, Chem. Commun. 50 (2014) 8941–8943.
[15] J. Zhao, T. Minegishi, L. Zhang, M. Zhong, M. Gunawan, G. Nakabayashi, T. Ma, M. Hisatomi, M. Katayama, S. Ikeda, N. Shibata, T. Yamada, K. Domen, Angew. Chem. Int. Ed. 53 (2014) 11808–11812.
[16] X. Sheng, L. Wang, L. Chang, Y. Luo, H. Zhang, J. Wang, D. Yang, Chem. Commun. 48 (2012) 4746–4748.
[17] K. Siemer, J. Klaer, I. Luck, J. Bruns, R. Klenk, D. Bräunig, Sol. Energy Mater. Sol. Cells 67 (2001) 159–166.
[18] X.J. Wu, X. Huang, X. Qi, H. Li, B. Li, H. Zhang, Angew. Chem. Int. Ed. 53 (2014) 8929–8933.
[19] L. Rovelli, S.D. Tilley, K. Sivula, ACS Appl. Mater. Interfaces 5 (2013) 8018–8024.
[20] C. Li, T. Ahmed, M. Ma, T. Edvinsson, J. Zhu, Appl. Catal. B: Environ. 138–139 (2013) 175–183.
[21] T. Jin, P. Diao, Q. Wu, D. Xu, D. Hu, Y. Xie, M. Zhang, Appl. Catal. B: Environ. 148–149 (2014) 304–310.
[22] J. Han, Z. Liu, K. Guo, B. Wang, X. Zhang, T. Hong, Appl. Catal. B: Environ. 163 (2015) 179–188.
[23] S. Emin, M. de Respinis, M. Fanetti, W. Smith, M. Valant, B. Dam, Appl. Catal. B: Environ. 166–167 (2015) 406–412.
[24] J. Han, Z. Liu, K. Guo, X. Zhang, T. Hong, B. Wang, Appl. Catal. B: Environ. 179 (2015) 61–68.
[25] J. Luo, S.D. Tilley, L. Steier, M. Schreier, M.T. Mayer, H.J. Fan, M. Grätzel, Nano Lett. 15 (2015) 1395–1402.
[26] A.B. Wong, S. Brittman, Y. Yu, N.P. Dasgupta, P. Yang, Nano Lett. 15 (2015) 4096–4101.
[27] N.P. Dasgupta, J. Sun, C. Liu, S. Brittman, S.C. Andrews, J. Lim, H. Gao, R. Yan, P. Yang, Adv. Mater. 26 (2014) 2137–2184.
[28] J. Tang, J. Huo, S. Brittman, H. Gao, P. Yang, Nat. Nanotechnol. 6 (2011) 568–572.
[29] W. Sheng, B. Sun, T. Shi, X. Tan, Z. Peng, G. Liao, ACS Nano 8 (2014) 7163–7169.
[30] L. Shi, P. Yin, L. Wang, Y. Qian, CrystEngComm 14 (2012) 7217–7221.
[31] J.J. Wu, W.T. Jiang, W.P. Liao, Chem. Commun. 46 (2010) 5885–5887.
[32] W. Yang, Y. Oh, J. Kim, H. Kim, H. Shin, J. Moon, ACS Appl. Mater. Interfaces 8 (2016) 425–431.
[33] S.T. Connor, C.M. Hsu, B.D. Weil, S. Aloni, Y. Cui, J. Am. Chem. Soc. 131 (2009) 4962–4966.
[34] X.J. Wu, X. Huang, X. Qi, H. Li, B. Li, H. Zhang, Angew. Chem. Int. Ed. 53 (2014) 8929–8933.
[35] L. Mu, F. Wang, B. Sadtler, R.A. Loomis, W.E. Buhro, ACS Nano 9 (2015) 7419–7428.
[36] D. Wu, J. Duan, C. Zhang, K. Guo, H. Zhu, J. Phys. Chem. C 117 (2013) 9121–9128.
[37] J. Xu, C.S. Lee, Y.B. Tang, X. Chen, Z.H. Chen, W.J. Zhang, S.T. Lee, W. Zhang, Z. Yang, ACS Nano 4 (2010) 1845–1850.
[38] S.R. Thomas, C.W. Chen, M. Date, Y.C. Wang, H.W. Tsai, Z.M. Wang, Y.L. Chueh, RSC Adv. 6 (2016) 60643–60656.
[39] S.H. Wang, S.H. Yang, Chem. Mater. 13 (2001) 4794–4799.
[40] X. Liu, M.T. Mayer, D. Wang, Angew. Chem. Int. Ed. 49 (2010) 3165–3168.
[41] L. Li, Z. Liu, M. Li, L. Hong, H. Shen, C. Liang, H. Huang, D. Jiang, S. Ren, J. Phys. Chem. C 117 (2013) 4253–4259.
[42] H. Chen, Z. Wei, K. Yan, Y. Bai, Z. Zhu, T. Zhang, S. Yang, Small 10 (2014) 4760–4769.
[43] M. Li, R. Zhao, Y. Su, Z. Yang, Y. Zhang, Nanoscale 8 (2016) 8559–8567.
[44] M. Li, R. Zhao, Y. Su, J. Hu, Z. Yang, Y. Zhang, Adv. Mater. Interfaces (2016), http://dx.doi.org/10.1002/admi.201600494.
[45] W. Gunawan, T. Septina, Y. Harada, S. Nose, A.C.S. Ikeda, Appl. Mater. Interfaces 7 (2015) 16086–16092.
[46] D.C. Pan, L.J. An, Z.M. Sun, W. Hou, Y. Yang, Z.Z. Yang, Y.F. Lu, J. Am. Chem. Soc. 130 (2008) 5620–5621.
[47] H.Z. Zhong, Y. Zhou, M.F. Ye, Y.J. He, J.P. Ye, C. He, C.H. Yang, Y.F. Li, Chem. Mater. 20 (2008) 6434–6443.
[48] Z. Yin, Z. Hu, H. Ye, F. Teng, C. Yang, A. Tang, Appl. Surf. Sci. 307 (2014) 489–494.
[49] J. Chang, E.R. Waclawik, CrystEngComm 15 (2013) 5612–5619.
[50] S. Wang, S. Yang, Z.R. Dai, Z.L. Wang, Phys. Chem. Chem. Phys. 3 (2001) 3750–3753.
[51] Y. Hou, F. Zuo, A.P. Dagg, J. Liu, P. Feng, Adv. Mater. 26 (2014) 5043–5049.
[52] Z. Bai, X. Yan, Y. Li, Z. Kang, S. Cao, Y. Zhang, Adv. Energy Mater. 6 (2016) 1501459.
[53] Y. Hamanaka, T. Kuzuya, T. Sofue, T. Kino, K. Ito, K. Sumiyama, Chem. Phys. Lett. 466 (2008) 176–180.
[54] A. Paracchino, V. Laporte, K. Sivula, M. Grätzel, E. Thimsen, Nat. Mater. 10 (2011) 456–461.
[55] A. Paracchino, N. Mathews, T. Hisatomi, M. Stefik, S.D. Tilley, M. Grätzel, Energy Environ. Sci. 5 (2012) 8673–8681.
[56] A. Kargar, Y. Jing, S.J. Kim, C.T. Riley, X. Pan, D. Wang, ACS Nano 7 (2013) 11112–11120.
[57] F. Yang, V. Kuznietsov, M. Lublow, C. Merschjann, A. Steigert, J. Klaer, A. Thomasand, T.S. Niedrig, J. Mater. Chem. A 1 (2013) 6407–6415.